Microscopic oxygen isotopic homogeneity/heterogeneity in the matrix of the Vigarano CV3 chondrite

Takuya Kunihiro,* Kazuhide Nagashima, and Hisayoshi Yurimoto

Department of Earth and Planetary Sciences, Tokyo Institute of Technology, Meguro, Tokyo 152-8551, Japan

Abstract—Two-dimensional $^{18}O/^{16}O$ isotopic analysis of the Vigarano matrix was conducted by secondary ion-imaging using a novel two-dimensional ion-imager. Quantitative oxygen-isotope images (isotopographs) of the Vigarano matrix show that ^{16}O-rich micrograins are scattered within ^{16}O-poor matrix. This heterogeneous O-isotopic distribution indicates that matrix is composed of different O-isotopic components that formed in different locations and/or at different times. However, the O-isotopic composition of groundmass in the matrix is the same as the bulk isotopic composition of the matrix within $\pm 5\%o$ uncertainty. The spatial resolution and isotopic precision of our technique should allow submicron-size objects (>0.2 μm) with extreme O-isotopic anomalous characteristics ($\delta^{18}O_{SMOW}$ ~250‰) to be detectable in isotopographs. Because the mean grain size of the matrix is ~0.2 μm, the inability to detect such O-isotopic anomalous objects indicates that isotopically anomalous micrograins (e.g., presolar grains) are extremely rare in the Vigarano matrix and that most objects in the matrix were formed in the solar nebula or in the parent body. *Copyright © 2005 Elsevier Ltd*

1. INTRODUCTION

Primitive meteorites (chondrites) preserve records of the physical and chemical processes that occurred during the earliest stages of solar-system evolution. Chondrites are comprised of three major components: refractory inclusions, mafic chondrules, and fine-grained, volatile-rich matrix. The proportions of these components vary in different chondrite groups. How such mineralogically diverse objects, which experienced distinct thermal histories, came to coexist in chondrites is a major challenge for models of the formation and early evolution of planetary materials in the solar nebula. After O-isotopic anomalies were observed in refractory inclusions (Clayton et al., 1973), many O-isotopic studies were made on microareas in individual grains in refractory (Ca-Al-rich) inclusions (CAIs; Yurimoto et al., 1994; McKeegan et al., 1998), amoeboid olivine aggregates (AOAs; Hiyagon and Hashimoto, 1999; Krot et al., 2002; Imai and Yurimoto, 2003), and chondrules (Maruyama et al., 1999; Russell et al., 2000; Yurimoto and Wasson, 2002). However, only bulk analyses have been collected from matrices (Clayton and Mayeda, 1999). O-isotopic studies of individual grains and the in situ O-isotopic distribution in matrices with permil order precision have not succeeded probably due to the small size of the components. In this study, we attempted to obtain the in situ distribution of oxygen isotopes, i.e., isotopography. We made high-precision isotope imaging analyses with micron-scale resolution (Yurimoto et al., 2003) of the Vigarano CV3 chondrite matrix.

Several pioneering studies were previously performed using an isotope mapping technique (Nittler et al., 1994, 1997; Hoppe et al., 2000; Aléon et al., 2001; Messenger et al., 2003; Mostefaoui et al., 2003; Strebel and Hoppe, 1999). The spatial resolution of these studies was on the micron to submicron level; however, the

precision of the isotope ratios was limited to several percent. Therefore, the application was limited to samples and nuclides having large isotopic anomalies such as presolar grains and interplanetary dust particles (IDPs).

There are two approaches to obtain an isotope map using secondary ion mass spectrometry (SIMS): scanning and direct imaging. The spatial resolution of the scanning approach depends on the size of the primary beam (e.g., Cameca NanoSIMS). With direct imaging, the stigmatic ion optics of SIMS generates mass-filtered ion images of the sample surface with micron scale spatial resolution irrespective of the size of the primary beam. This direct imaging technique has the definite advantage of shorter acquisition times. The most popular two-dimensional direct imaging-system consists of a microchannel plate (MCP), a fluorescent screen (FS), and a charge coupled device (CCD). Although this detection system is highly sensitive, it is difficult to achieve quantitative isotopic measurements because of nonlinearity in electron-to-photon conversion factor of the FS, narrow dynamic range of FS, and time dependent change of conversion efficiency of FS and MCP which is caused by damage from electron or ion bombardment.

Recently, a stacked CMOS-type active pixel sensor for charged particles (SCAPS) was developed (Matsumoto et al., 1993; Takayanagi et al., 2003). Because the SCAPS is composed of a pixelled array of ~600 × 600 independent microdetectors, simultaneous two-dimensional detection can be achieved. The SCAPS is suitable for high-precision-isotope imaging, isotopography, because of its direct ion-capability, high sensitivity, low noise, and wide dynamic range (Nagashima et al., 2001; Kunihiro et al., 2001; Takayanagi et al., 2003). Secondary ion intensities can be determined within twice the Poisson statistical error. The readout limit of the SCAPS corresponds to 3 ions per pixel and the accumulation limit corresponds to 3×10^5 ions per pixel.

Kunihiro et al. (2002) reported microscale O isotopographs of chondrite matrices and discussed the usefulness of isotopog-

---

* Author to whom correspondence should be addressed, at Department of Earth and Space Sciences, University of California, Los Angeles, CA 90095-1567, USA (tky@ess.ucla.edu).

Table 1. Measurement conditions of isotopography.

Area	Size (μm^2)	Measured ion	Average ion numbers per pixel per cycle (integration time)				Cycles
			$^{16}O^-$	$^{17}O^-$	$^{18}O^-$	$^{28}Si^-$	
TTV3-1-01	30×30	$^{16}O^-, {}^{17}O^-, {}^{18}O^-, {}^{28}Si^-$	2×10^4 (40 s)	3×10^2 (1600 s)	7×10^2 (700 s)	5×10^2 (80 s)	1
TTV3-1-02	70×70	$^{16}O^-, {}^{18}O^-, {}^{28}Si^-$	3×10^4 (40 s)	—	6×10^2 (530 s)	4×10^2 (80 s)	4
TTV3-1-03	80×80	$^{16}O^-, {}^{18}O^-, {}^{28}Si^-$	3×10^4 (40 s)	—	5×10^2 (380 s)	5×10^2 (80 s)	1

raphy. In this paper we apply isotopography to the matrix of the Vigarano CV3 chondrite and demonstrate that oxygen isotopes are heterogeneously distributed in the Vigarano matrix. We show that most objects in the matrix were formed in the solar nebula or on the parent body.

2. EXPERIMENTAL PROCEDURES

2.1. Sample

The sample used in this study is a polished thin section (TTV3-1) of the Vigarano CV3 meteorite. The sample was coated with a 40-nm-thick layer of carbon film. Petrologic and mineralogical studies were made in parts of the matrix in the thin section using a scanning electron microscope (JEOL JSM-5310LV) equipped with an energy dispersive X-ray spectrometer (Oxford LINK-ISIS). Quantitative analyses were carried out at an accelerating voltage of 15 kV and a 1-nA probe current. We selected three typical matrix areas from the thin section (TTV3-1-01, -02, and -03) for isotopography. The total area of the three images is 12,000 μm^2. Following Lee et al. (1996), we use the term "matrix" for the micron- to submicron-scale fine-grained materials that lie between such objects as chondrules, chondrule fragments, and refractory inclusions that are normally hundreds of microns in size. Petrographic studies were made before and after the isotope analysis.

2.2. SIMS Operating Conditions for Spot Analysis

Spot analyses for O-isotopes were carried out using the Cameca IMS-1270 SIMS instrument at Tokyo Institute of Technology (TiTech). The primary ion beam consisted of mass-filtered 20 keV Cs^+ ions, focused to a spot size of 3 μm. The primary beam current was ~3 pA, adjusted to obtain a count rate of ~4 × 10^5 cps for $^{16}O^-$ ions. A normal incidence electron gun was used for charge compensation. Negative secondary ions corresponding to the $^{16}O^-$ tail, $^{16}O^-$, $^{17}O^-$, $^{16}OH^-$, and $^{18}O^-$ were analyzed at a mass resolution of ~6000 (10% valley). Additional information on the analytical procedure is given in Yurimoto et al. (1998).

2.3. Isotopography: High Precision Isotope Ratio Microimaging

Isotopographs of O-isotope ratios were obtained by the TiTech isotope microscope (Cameca IMS-1270 ion microscope equipped with SCAPS imaging system; Yurimoto et al., 2003).

A 20-keV Cs^+ primary ion beam was rastered over a 130×130 μm^2 sample area to achieve uniform secondary ion-beam emission from an imaging area of 75×75 μm^2. A normal incident electron gun was used for charge compensation of the rastered area. The primary current was adjusted to ~0.5 nA to obtain a count rate of ~1 × 10^8 cps for $^{16}O^-$ ions total to irradiate to the SCAPS device. The secondary ions were accelerated to −10 keV and measured as mass-filtered ion images projected by the stigmatic ion optics of the Cameca IMS-1270 instrument. The ion microscope was operated with 150 μm transfer optics and a 2×2 to 6×6 mm^2 field aperture giving a 30×30 to 80×80 μm^2 field of view. A 150 μm diameter focal plane aperture was used and the width of the energy bandpass was set to ±75 eV. The exit slit was narrowed to minimize the contribution of $^{16}OH^-$ to the isotopic image of $^{17}O/^{16}O$ (M/ΔM = ~6000, 10% valley). The SCAPS device was positioned on the projection plane of the mass-filtered secondary ion image.

The SCAPS is a novel solid-state ion imager. The operational principle of SCAPS is based on detecting the change in potential of a floating capacitor, as caused by charged particle irradiation. The SCAPS is composed of a pixel array and scanning electronics. As the pixel array consists of 600×576 rectangle microdetectors, simultaneous two-dimensional detection for charged particles and/or high energy particles is achieved. The SCAPS is designed with pixel dimensions of 20×20 μm^2, and pixel electrode dimensions of 12.0×11.5 mm^2, yielding a fill factor of 88% (Takayanagi et al., 2003).

The SCAPS has several advantages over conventional detection systems including two-dimensional detection, wide dynamic range, no dead time, direct detection of charged particles, and constant ion-detection sensitivities among nuclides. Integrating detectors capable of storing charge are suitable for precise low-intensity measurements given a sufficient time period for integration, and can reduce statistical errors. As SCAPS has no period of insensitivity and is robust against ions, it is possible to measure incident charged particles with both high and low intensities, distributed in two dimensions, in the same time interval and under the same analytical conditions without any danger of mechanical or electronic damage, whereas conventional pulse count detectors are limited with regard to beam intensity.

The ion signal from the SCAPS was read out at a scan rate of 20 kilopixels per second. The signals from each pixel were amplified by a low-noise amplifier (Analog Devices, SSM-2017) and converted into a digital signal by a 16-bit A/D converter (Datel, ADS-930MC) in the external readout circuit, and the digital signals were processed using software developed in LabVIEW (National Instruments). To reduce environmental noise, the communications between the SCAPS and the operation electronics were by differential signals connected by shielded twisted-pair cables through an ultrahigh vacuum electrical feed-through. To control the dark current of the pixels the temperature of the device was cooled by liquid nitrogen.

After removing the carbon coating on the sample surface (presputtering) and obtaining stable secondary beam emission, ion images were detected by the SCAPS using the operation sequence described in Nagashima et al. (2001). The typical mass sequence for acquiring secondary ion images was $^{28}Si^-$, $^{16}O^-$, $^{18}O^-$, $^{16}O^-$, $^{17}O^-$, and $^{16}O^-$ for one cycle. The second $^{16}O^-$ and $^{17}O^-$ images were skipped when the $^{17}O/^{16}O$ isotopograph was not pursued. Typical integration times for these secondary ion species in one cycle were 80 s, 20 s, 500 s, 20 s, 1600 s and 20 s, respectively. Images of $^{16}O^-$ were acquired repeatedly throughout a cycle to correct for signal fluctuation, due to instrumental drift. We used an average $^{16}O^-$ image calculated before and after the $^{17}O^-$ or $^{18}O^-$ image to obtain the O-isotope ratio image. The sputtering depth of one cycle was less than 50 nm.

Linearity (Nagashima et al., 2001) and reset-frame (Kunihiro et al., 2001) corrections were applied to obtain ion counts from the outputs of the SCAPS. The procedure is as follows: (1) Detector reset: each pixel is reset by a destructive readout operation. (2) Offset frame read: signals from individual pixels are read by a nondestructive readout (NDRO) operation. The linearity correction is applied to individual pixel-signals. (3) Integration: charged particles are irradiated on the SCAPS. (4) Ion-integrated frame read: ion-integrated frames are read by the NDRO operation and linearity correction is applied. (5) Reset-frame correction: subtracting the offset frame from the ion-integrated frame extracts the total accumulated signal in each pixel that is proportional to number of incident ions. The individual conditions of each analyzed area are shown in Table 1.

Isotopographs were obtained by calculating $^{17}O^-/^{16}O^-$ and/or $^{18}O^-/^{16}O^-$ ratios for each pixel. However, normalization corrections are necessary to convert the relative secondary-ion-intensity ratios to δ-notation values because the raw ratios include uncertainties caused by
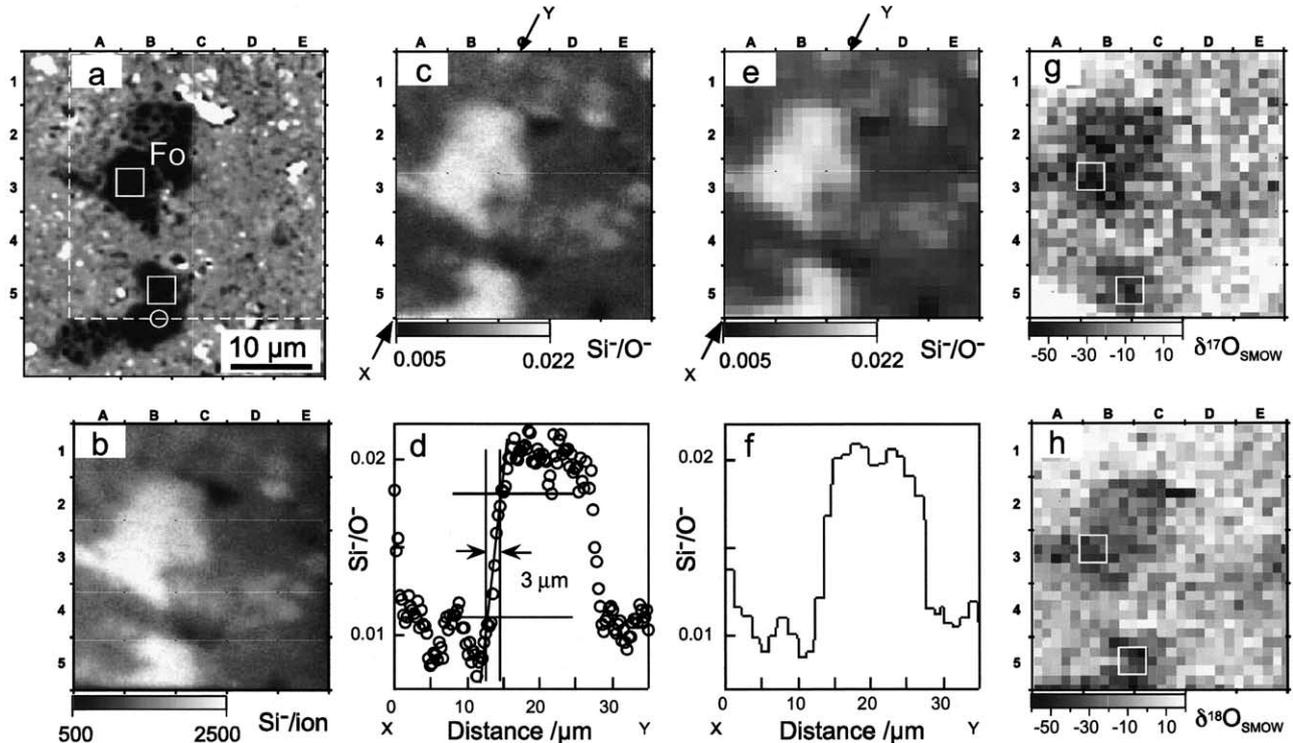
Fig. 1. (a) BSE image from TTV3-1-01. MgO-rich olivine grains consist of Fo93-95 with fayalitic rims. They are embedded in groundmass materials. Isotopographs of dashed area are shown in (b), (c), (e), (g) and (h). (b) Si$^-$ ion image. (c) Si$^-$/O$^-$ image. (d) Line profile for the Si$^-$/O$^-$ ratio between arrows X and Y in (c). Spatial resolution of the image is defined by the width of the signal change from 16 to 84% at the boundary. (e) Si$^-$/O$^-$ image after 5 × 5 pixels binning. (f) Line profile for the Si$^-$/O$^-$ ratio between arrows X and Y in (e). (g) Isotopograph of $\delta^{17}O_{SMOW}$. (h) Isotopograph of $\delta^{18}O_{SMOW}$. Olivine grains enriched in ^{16}O are observed.

time drift of secondary-ion emission and instrumental mass fractionation (Yurimoto et al., 2003). We used the Vigarano whole rock values determined by Clayton and Mayeda (1999; $\delta^{17}O_{SMOW} = -3.61‰$, $\delta^{18}O_{SMOW} = 1.19‰$) for the normalization because there are no reports for Vigarano matrix. The average of secondary-ion-intensity ratios of O isotopes in an image was normalized to the whole rock value. The difference in matrix effect between different minerals and heterogeneous instrumental mass fractionations within an image have not been corrected by the normalization procedure, and are evaluated in the following sections.

3. RESULTS

3.1. Performance and Quality of Isotopography

We evaluated the performance of SCAPS isotopography by examining olivine grains several microns in size (Fig. 1). A $^{28}Si^-$ image corresponding to the area outlined by the dashed line in Figure 1a is shown in Figure 1b. The $^{28}Si^-$ image shows that the distribution of secondary-ion emission from olivine grains is slightly heterogeneous. The heterogeneous pattern of ion emission changes with the location of incident electron-beam on the sample surface. Therefore the heterogeneous emission pattern mainly reflects small variations in charging status on the sample surface, which corresponds to incomplete charge compensation. This is probably caused by a heterogeneously distributed electron-beam generated by the normal incident electron-gun. Such analytical artifact patterns can be corrected if we use the secondary-ion-intensity ratio, Si$^-$/O$^-$, instead of the secondary-ion intensity (Fig. 1c) to reproduce images.

The Si$^-$/O$^-$ ratio-variations between the arrows of Figure 1c (line X-Y) are shown in Figure 1d. From the sharpness of the boundary between the forsterite grain and the surrounding area, we can determine the spatial resolution of the isotopograph. The spatial resolution defined by the width for the signal changes from 16 to 84% is calculated to be 3 μm. Therefore, pixel binning with 5 × 5 pixels (1.25 × 1.25 μm^2 on sample surface) was applied to reduce noise coming from the statistical fluctuation in secondary-ion intensity (Figs. 1e,f). Although the number of pixels in the binned image was reduced to 1/25 of the original image, the spatial information was not significantly reduced because the spatial resolution of 3 μm corresponds to 12 pixels. This pixel-binning technique is also applied to the isotopographs of $^{17}O/^{16}O$ (Fig. 1g) and $^{18}O/^{16}O$ (Fig. 1h). ^{16}O-enrichments of the forsterite grains relative to the surrounding area were observed in the images (Figs. 1g,h).

Quantitative confirmation of the ^{16}O-enrichments in the forsterite was made by comparing the values obtained by spot analysis and the isotopograph. A spot analysis was made at the location marked by an open circle in square B5 of Figure 1a. The results are compared with those obtained for 3 × 3 pixel areas in squares B3 and B5 in the isotope-ratio images (Figs. 1a,g,h). The uncertainty of the O-isotope ratio for one pixel is estimated as the standard deviation (1σ) of the $^{17}O/^{16}O$ and $^{18}O/^{16}O$ ratios among the nine binned pixels. The δ-values for forsterite determined by isotopography are in good agreement (i.e., within analytical uncertainty) with the results of the

Table 2. O-isotope data (‰) of olivine grains in area TTV3-1-01.

Micro object	Location in Fig. 1	Method	$\delta^{17}O_{SMOW}$	$1\sigma_{mean}$	$\delta^{18}O_{SMOW}$	$1\sigma_{mean}$
O1-01 (Fo93)	B5	Spot	−42	2[a]	−32	1[a]
O1-01 (Fo93)	B5	Imaging	−37	8[b] (13[c])	−36	11[b] (8[c])
O1-02 (Fo95)	B3	Imaging	−46	13[b] (13[c])	−36	6[b] (8[c])

[a] Standard error: calculated from standard deviation of one measurement series and the number of measurement cycles.
[b] Standard deviation in isotopograph: standard deviation of nine binned-pixels from the isotopograph.
[c] Statistic error: calculated from the accumulated ion numbers in one binning-pixel.

spot analysis (Table 2). The uncertainty of the SCAPS analysis is consistent with the calculated statistical uncertainties from the number of accumulated ions in a SCAPS pixel.

In this analytical condition, $^{16}OH^-$ intensities were typically 10× larger than $^{17}O^-$ intensities. A slit at the mass-dispersion plane (exit slit) was narrowed to minimize the contribution of $^{16}OH^-$ to the isotopograph of $^{17}O/^{16}O$ (Fig. 2a). The boundary between arrows of U and D corresponds to the edge of the exit slit at high-mass side. The mass spectrum along the horizontal line (X–Y) of the exit-slit image shows the $^{17}O^-$ peak and the low-mass side tail of $^{16}OH^-$ peak (Fig. 2b). The total number of ions from the $^{16}OH^-$ tail is less than ~2% relative to that from the $^{17}O^-$ peak. Most of the $^{16}OH^-$ ions located at the low-mass side of the $^{16}OH^-$ peak are projected onto the lower left corner (and upper right corner) of the stigmatic ion image in the projection plane because of second-order aberrations in the ion optics of the Cameca ion-microscope. The contribution of the interference at the lower left and upper right corners in an isotopograph varies depending on the tuning of the ion optics. With the instrumental condition used in this study, the interference only appeared in the lower left corner (square A5 of Fig. 1g). Most of the interference is concentrated in the A5 area, and the signal here is dominated by interference. The contribution is roughly estimated as follows: The dimension of the region where $^{16}OH^-$ ions were projected into is estimated to be 1/25 of the whole $^{17}O^-$ image. Since the ~2% contribution of $^{16}OH^-$ to $^{17}O^-$ is concentrated in 1/25 of the area, the contribution of $^{16}OH^-$ to $^{17}O^-$ image in the square A5 in Figure 1g is calculated to be ~50% (= 25 × 2%). This is consistent with the $\delta^{17}O_{SMOW}$ value (~500‰) in square A5 in Figure 1g. Such contribution due to interferences in other secondary ion-images were less than 0.1‰ for each pixel and can be ignored in this study.
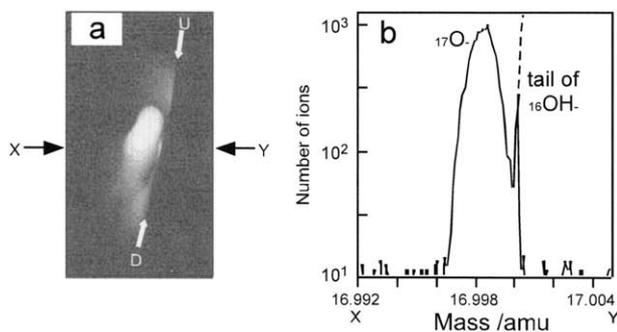

Fig. 2. (a) Slit image of $^{17}O^-$. The curve between the arrows U and D corresponds to the edge of the exit slit at the low-mass side. (b) Mass spectrum between X and Y. M/ΔM = ~6000 (10% valley).

3.2. Characteristics of Oxygen Isotope Distribution in Matrix

Lee et al. (1996) reported that Vigarano matrix was dominated by Mg-Fe silicates, mainly olivines, which were subdivided into two groups on the basis of grain size, micro-objects (>2 μm) and submicro-objects (<0.5 μm). Submicro-objects and the interstitial materials form a groundmass surrounding micro-objects. Zolensky et al. (1993) reported compositional heterogeneities in the matrix groundmass, with the MgO/(MgO + FeO) × 100 [Fo] ranging from 32 to 52. Micro-objects were normally classified as MgO-rich olivine, FeO-rich olivine, low-Ca pyroxene, and augite. These descriptions for the matrix are consistent with our observations in this study. The size of each micro-object in this study was 2 to 10 μm across. We use the terms of MgO-rich olivine and FeO-rich olivine for the compositions greater than and less than Fo60, respectively.

Using this definition, the large olivine grains in the area TTV3-1-01 (Fig. 1) are categorized as MgO-rich micro-objects. The micro-objects consist of forsterite (Fo93-95) with thin fayalitic rims (<1 μm thickness); they are embedded in a groundmass of olivine with ~Fo52. The O-isotope composition of the micro-objects is clearly ^{16}O-rich while the groundmass is ^{16}O-poor. It is not clear if the fayalitic rim is ^{16}O-poor or ^{16}O-rich because of the limited resolution of the isotopograph.

Figure 3a shows a backscattered-electron image of an analyzed area, TTV3-1-02, of the Vigarano matrix. A micron-scale CAI lies in the groundmass (Fig. 3a, B2). The spinel grains are rimmed by a Ca-bearing phase, probably diopside (Fig. 4a). The TTV3-1-02 area also contains micro-objects of MgO-rich olivine (Fo66–87; Figs. 4a–d), FeO-rich olivine (Fo40–44; Fig. 3, A2, B4, D5, Fig. 4c, A5, and Fig. 4d, C4), and low-Ca pyroxene. Each MgO-rich micro-object consists of a MgO-rich core surrounded by a ~1-μm-thick fayalitic rim. The fayalitic rims have irregular shapes. The FeO-rich-olivine micro-object does not contain a MgO-rich core but the shape is irregular, similar to that of the fayalitic rim. The chemical composition of the FeO-rich-olivine micro-object is identical to that of the fayalitic rim. The sizes of micro-objects in this area range from 2 to 6 μm. The micro-objects are enclosed by groundmass that is mainly composed of submicron-sized olivine (representative size ~0.2 μm) with ~Fo37.

Figure 3b shows the Si^-/O^- ratio image of the analyzed area. Intensity ratios of the Si^-/O^- help to identify phases in the BSE image and the isotopograph. Dark objects in square B2 of Figure 3b correspond to spinel in the micro-CAI in square B2 of Figure 3a. White objects correspond mainly to olivine and low-Ca pyroxene. The isotopograph of $^{18}O/^{16}O$ in this area is shown in Figure 3c. The isotopograph directly shows that ^{16}O-rich grains
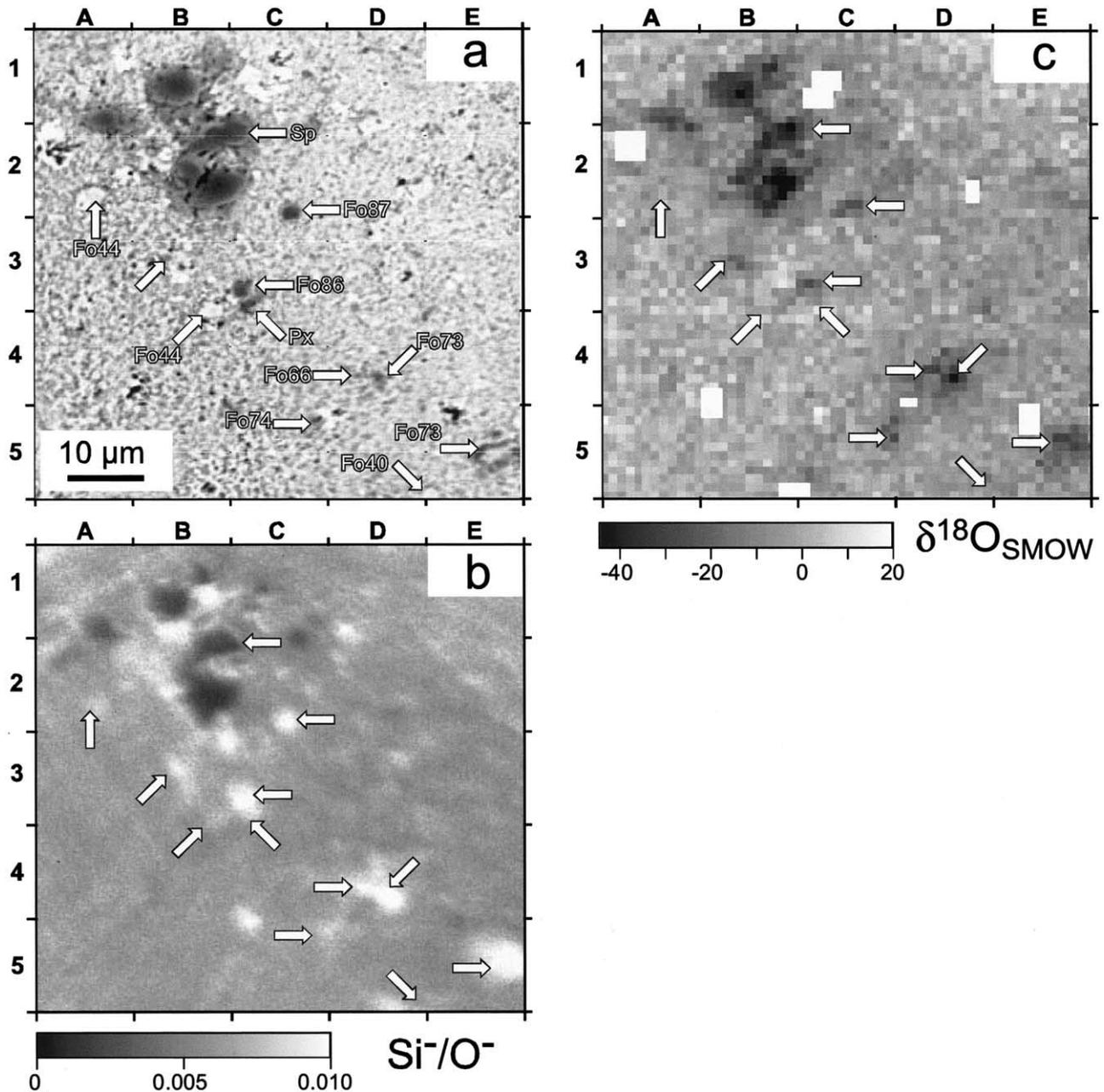
Fig. 3. (a) BSE image from TTV3-1-02. (b) Si^-/O^- image of corresponding area. (c) Isotopograph of $^{18}O/^{16}O$ after pixel-binning technique was applied. The locations of micro-objects in the Si^-/O^- image and isotopograph of $\delta^{18}O_{SMOW}$ are indicated by arrows in (b) and (c), respectively. Sp = spinel; FoX = olivine with forsteritic content X [=MgO/(MgO + FeO) × 100]; Px = low-Ca pyroxene. The isotopograph shows that O isotopes are distributed heterogeneously in the matrix. Spinel in the refractory inclusion and MgO-rich-olivine micro-objects in this area are clearly enriched in ^{16}O. The standard deviation $\delta^{18}O_{SMOW}$ in the groundmass area is estimated to be 5‰ and this is consistent with the calculated statistical uncertainty. Pixels with white color in (c) correspond to metal or sulfide grains, or holes on the surface. These areas have no oxygen or yield irregular secondary-ion emissions.

are scattered in the matrix. Spinel and diopside in the CAI and MgO-rich-olivine micro-objects marked by arrows in Figure 3c are clearly enriched in ^{16}O ($\delta^{18}O_{SMOW} \sim -40‰$) but the O-isotope compositions of the fayalitic rims cannot be determined because of the limited resolution of the O isotopograph. The smallest MgO-rich micro-object enriched in ^{16}O ($\delta^{18}O_{SMOW} \sim -40‰$) that we observed is ~2 μm across. The O-isotopic

compositions of the ^{16}O-rich micro-objects in this area are shown in Table 3. The ^{16}O-rich spot observed in B3 (Fig. 3c) also corresponds to a tiny MgO-rich olivine grain; however it is not listed in Table 3 because it was too small to measure its FeO content.

All low-Ca pyroxene and FeO-rich-olivine micro-objects in area TTV3-1-02 have ^{16}O-poor characteristics. One excep-
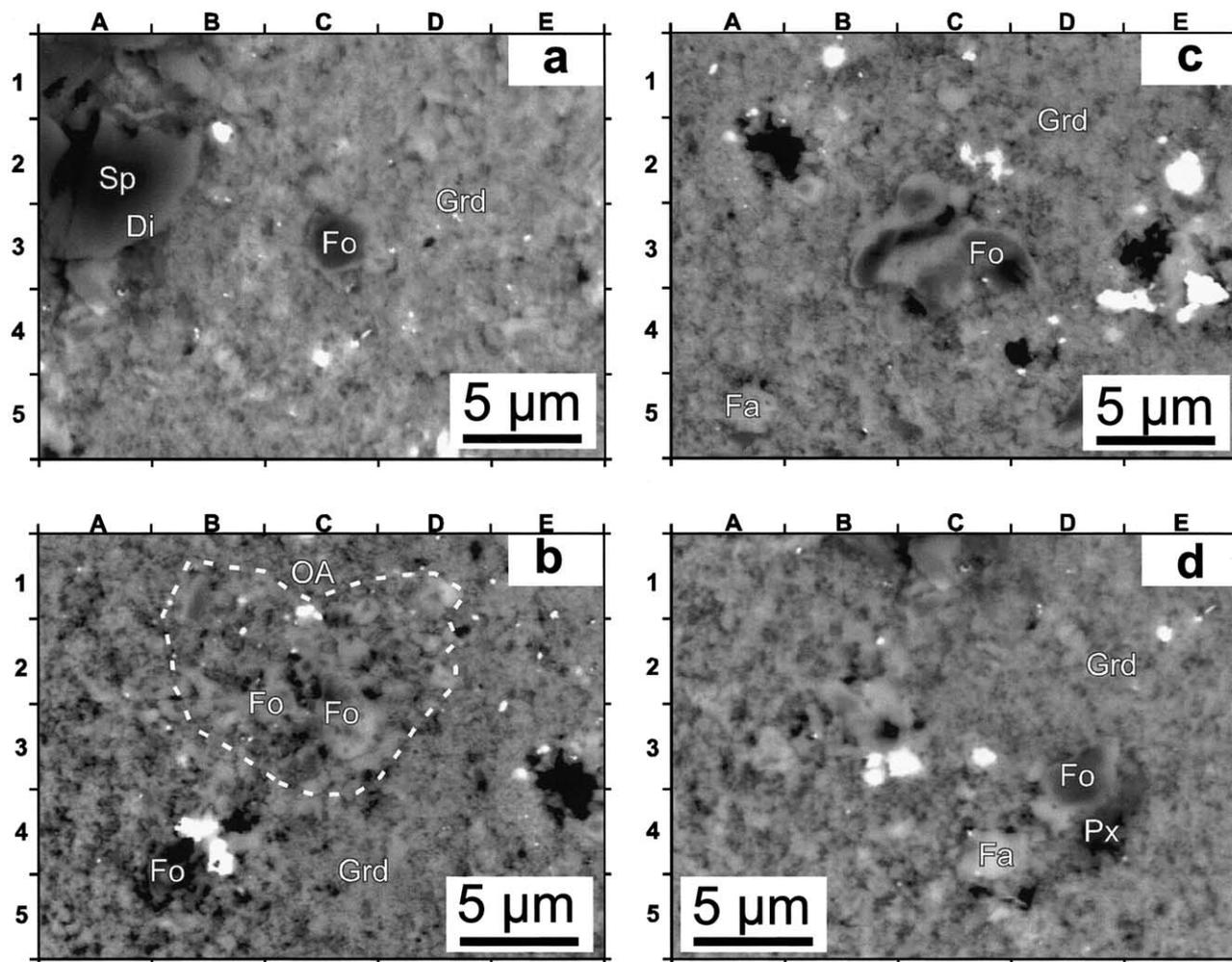
Fig. 4. High-magnification BSE-images from TTV3-1-02 corresponding to area (a) C2, (b) D4, (c) E5 and (d) B3 of TTV3-1-02 (Fig. 3a). The locations of micro-objects in the Si^-/O^- image and isotopograph of $^{18}O/^{16}O$ are indicated by arrows in Figures 5b and 5c, respectively. Fo = MgO-rich olivine micro-object; Fa = FeO-rich olivine micro-object; Px = low-Ca pyroxene; Sp = spinel; Di = diopside; Grd = groundmass; OA = olivine aggregate.

tional group of FeO-rich olivine grains occurs in square D4 of Figure 3. We found that these FeO-rich olivine grains of submicron size constitute an olivine aggregate (Fig. 4b). Some of the FeO-rich olivines contain small MgO-rich cores. O-isotope compositions of the cores (Fo66-74) of the micro-objects (>2 μm) in this aggregate are $\delta^{18}O_{SMOW} \sim -40\%o$ (Table 3). Although the spatial resolution of the isotopograph is limited, it seems that the parts of the olivine aggregate that are moderately enriched in FeO also show ^{16}O-rich characteristics. The bulk O-isotopic composition of the olivine aggregate is calculated to be $\delta^{18}O_{SMOW} \sim -23\%o$.

The groundmass is isotopically homogeneous and ^{16}O-poor (Fig. 3c). The standard deviation of $\delta^{18}O_{SMOW}$ in the groundmass area is estimated from binned pixels and calculated to be 5‰. This is consistent with the calculated statistical uncertainty from accumulated ion numbers in a SCAPS pixel, 4‰.

Figure 5a shows a backscattered-electron image of another area (TTV3-1-03) of the Vigarano matrix. This area contains micro-objects of MgO-rich olivine (Fo91-94), augite, and low-Ca pyroxene. These MgO-rich-olivine micro-objects are surrounded by fayalitic rims. They are enclosed by groundmass with ~Fo44. Figure 5b shows the Si^-/O^- ratio image of the analyzed area. The locations of micro-objects in the Si^-/O^- and $^{18}O/^{16}O$ ratio images are shown by arrows in Figures 5b and 5c, respectively. Random noise in the isotopograph in Figure 5c is slightly larger than in Figure 3c because of the shorter accumulation times (Table 1). All micro-objects in this area are depleted in ^{16}O ($\delta^{18}O_{SMOW} \sim 0\%o$; Table 4). The fayalitic rim surrounding the MgO-rich olivine micro-object also seems to be ^{16}O-poor. The O isotopograph shows that $^{18}O/^{16}O$ ratios are homogeneously distributed in the groundmass. The standard deviation of $\delta^{18}O_{SMOW}$ in the groundmass area is calculated to be 10‰; corresponding to statistical uncertainty of 9‰ determined from the number of accumulated ions in a SCAPS pixel.

The relationship between the O-isotope composition and the Fo content of olivine micro-objects in this study is shown in Figure 6. The Fo contents of the olivine micro-object are distributed bimodally [FeO-rich (Fõ40) and MgO-rich (Fo >70)]. Micro-objects consist of clearly defined ^{16}O-rich and ^{16}O-poor parts.

Micro-object	Location in Fig. 3	Diameter/μm	$\delta^{18}O_{SMOW}$	$1\sigma_{mean}$
Sp-01	B1	4	−36	5
Sp-02	B2	3	−37	5
Sp-03	B2	5	−41	5
O1-03 (Fo87)	C2	2	−26	5
O1-04 (Fo86)	C3	2	−27	5
O1-05 (Fo73)	E5	2	−26	5
O1-06 (Fo44)	A2	3	−1	5
O1-07 (Fo40)	D5	2	−3	5
O1-08 (Fo44)	B4	2	4	5
O1-09 (Fo73)	D4	3	−43	5
O1-10 (Fo66)	D4	2	−30	5
O1-11 (Fo74)	C5	2	−29	5
Px-01	C3	2	−6	5
OA-01	D4	10	−23	5

[a] Sp = spinel; Ol = olivine; Px = low-Ca pyroxene; OA = olivine aggregate.

4. DISCUSSION

4.1. Performance and Quality of Isotopograph

Oxygen isotopographs in this study show the following characteristics: (1) No systematic spatial pattern is observed within any isotopograph even in the groundmass image (Figs. 1, 3 and 5). (2) Standard deviations ($1\sigma_{mean}$) of the O-isotope compositions observed in the olivine grains are consistent with the statistical uncertainty ($1\sigma_{mean}$) estimated from the number of accumulated ions in a pixel (Table 2). (3) The difference in O-isotope compositions between the FeO-rich groundmass and MgO-rich-olivine micro-object determined by isotopography are in good agreement with those determined by spot analysis (Fig. 1 and Table 2). According to these observations, the matrix effect among minerals and the heterogeneities of instrumental mass fractionation within an image should be smaller than the uncertainty of isotopography (<5‰) which is equivalent to the statistical error. The small matrix effect and small variation of instrumental mass fractionation within an image observed in this study are consistent with the results of Yurimoto et al. (2003).

The diameters of MgO-rich micro-objects located in C2, C3, C5, D4 and E5 (TTV3-1-02; Fig. 3) are ~2 μm; the objects have $\delta^{18}O_{SMOW}$ ~ −30‰ (Table 3 and Fig. 6). Because the spatial resolution is 3 μm in the isotopograph, the $\delta^{18}O_{SMOW}$ value of −30‰ determined for the MgO-rich olivine micro-objects is probably affected by O isotopes from the surrounding area (which is ^{16}O-poor). The true $\delta^{18}O_{SMOW}$ value of the MgO-rich micro-objects seems to be about −40‰.

4.2. Origin of the Matrix

Using the O-isotopic compositions, components of the Vigarano matrix can be classified into ^{16}O-rich and ^{16}O-poor groups corresponding to $\delta^{18}O_{SMOW}$ values of ~ −40‰ and ~0‰ (Fig. 6). There is no simple correlation between the degree of ^{16}O-enrichment and FeO content.

It is clear that MgO-rich-olivine micro-objects in the matrix were derived from two distinct O-isotope reservoirs. The ^{16}O-rich MgO-rich micro-objects are related to AOAs (amoeboid olivine aggregates; Hiyagon and Hashimoto, 1999; Krot et al.,

2002; Imai and Yurimoto, 2003) and the ^{16}O-poor ones are either related to chondrules or formed on the CV parent-body (Clayton, 1993; Imai and Yurimoto, 2003). This two-component-mixing model is partly supported by the presence of a micro CAI (Fig. 3). Therefore some of the MgO-rich micro-objects may be fragments of AOAs or chondrules.

Each MgO-rich-olivine micro-object is surrounded by a ~1 μm thick fayalitic rim. Because the FeO content of the rim is fairly constant and changes abruptly at the boundary between the core and rim (Figs. 4a, C3, 4c, C3, and 4d, D3), it is clear that interdiffusion of Fe-Mg in the original olivine grain is not the main process for forming the fayalitic rim. However, overgrowth of the fayalitic rim on an original MgO-rich micro-object is plausible. FeO-rich and ^{16}O-poor irregularly shaped olivine micro-objects (<2 μm in diameters) that lack a MgO-rich core occur in the matrix (Fig. 4c, A5; Fig. 4d, C4). The chemical compositions of these FeO-rich-olivine micro-objects are similar to those of the fayalitic rim and groundmass olivine in the matrix, indicative of chemical equilibrium. From these observations and the discussion of Imai and Yurimoto (2003), we conclude that the ^{16}O-poor FeO-rich-olivine micro-objects and the FeO-rich rim around MgO-rich-olivine micro-objects formed in the parent body.

Although the FeO content abruptly changes at the core-rim boundary of the olivine micro-objects, narrow diffusion profiles of Fe (~0.5 μm) are observed in the boundary (Figs. 4a, C3, 4c, C3, and 4d, D3). Vigarano has undergone limited hydrothermal alteration and the matrix was affected by mild aqueous alteration at low temperatures (Lee et al., 1996). Using the estimated peak temperature of the Vigarano parent-body (400 to 500 °C) and the Fe-Mg diffusion coefficients determined by Chakraborty (1997), we find that annealing for $3 \times 10^{3-5} \times 10^{5}$ yr is necessary to form the Fe-Mg diffusion profiles. This annealing duration seems to be consistent with the alteration period in the parent body. A hydrothermal alteration in the parent body (Krot et al., 1995, 1998) seems to be the dominant process for the formation of the FeO-rich micro-objects.

Because the O-diffusion rate in olivine is much slower than the Fe-Mg diffusion rate (Buening and Buseck, 1973; Jaoul et al., 1980, 1983; Reddy et al., 1980; Gérard and Jaoul, 1989; Ryerson et al., 1989; Chakraborty, 1997), the O-isotope fea-
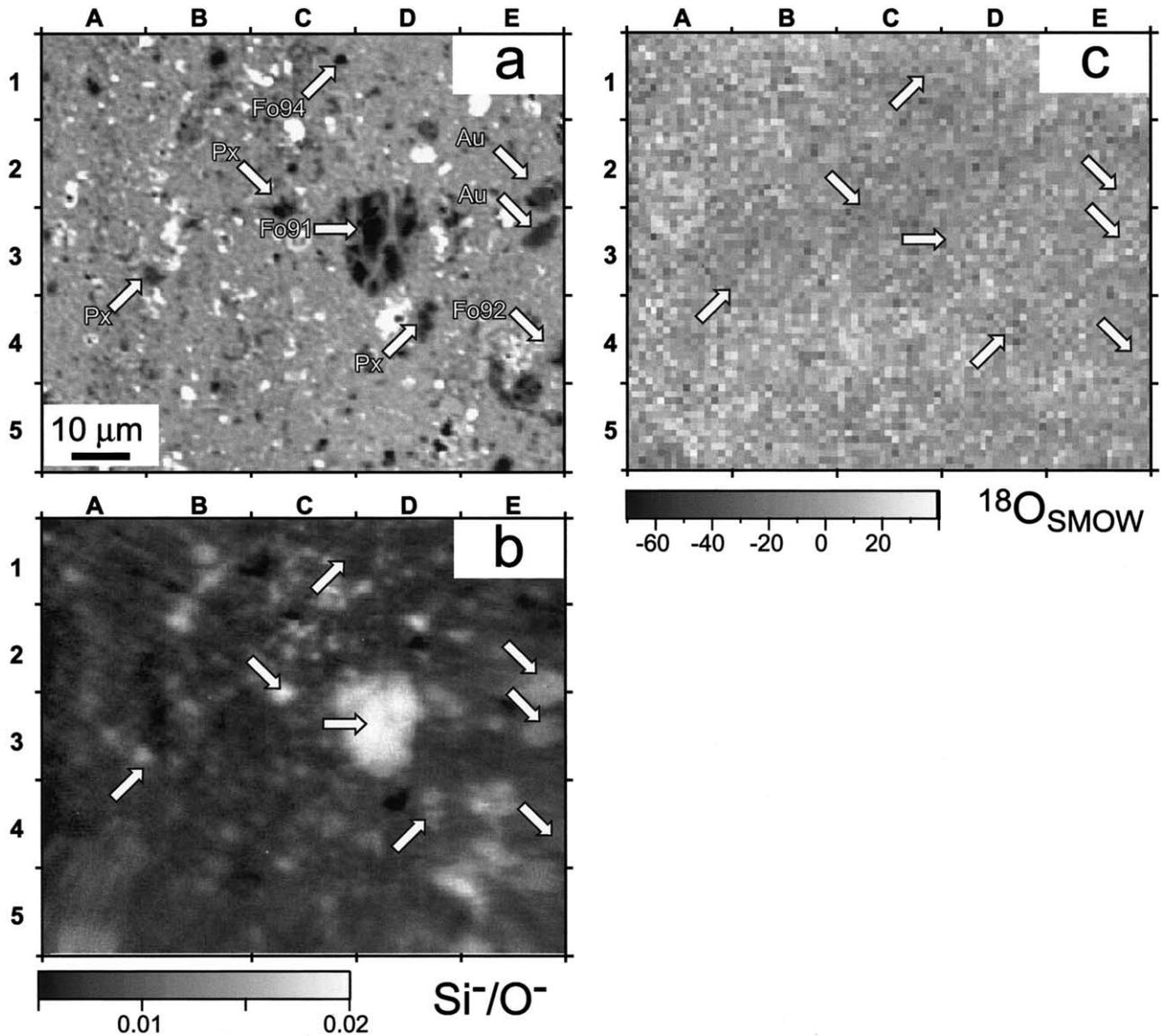
Fig. 5. (a) BSE image from TTV3-1-03. (b) Si^-/O^- image of corresponding area. (c) Isotopograph of $^{18}O/^{16}O$ after the pixel-binning technique was applied. FoX = olivine with foresteritic content X; Px = low-Ca pyroxene; Au = augite. The isotopograph shows that oxygen isotopes are distributed homogeneously in this area. The standard deviation $\delta^{18}O_{SMOW}$ in the groundmass area is estimated to be 10‰ and this is consistent with the calculated statistical uncertainty.

tures in MgO-rich micro-objects should be retained during thermal processing in the parent body. The length of O-diffusion relative to that of Fe-Mg varies depending on temperature, i.e., O-diffusion lengths between 400 and 500°C change by a factor of 22, and Fe-Mg-diffusion lengths change by a factor of 14 over this temperature range (Ryerson et al., 1989; Chakraborty, 1997). Effects of oxygen fugacity (fO_2) for relative diffusion lengths between these elements are proportional to $fO_2^{0.02}$ (Buening and Buseck, 1973; Ryerson et al., 1989) and are small if we can assign Fe-Mg diffusion lengths. As a result, because the Fe-Mg diffusion length observed in the olivine grains is ~0.5 μm, the O-diffusion length can be estimated to be <1 nm using diffusion coefficients of O and Fe-Mg (400 to 500°C; Ryerson et al., 1989; Chakraborty, 1997). This prediction is consistent with the O isotopography

showing that olivine micro-objects of 2 μm retained their original ^{16}O-rich features.

A FeO-rich olivine-aggregate with moderately ^{16}O-rich characteristics ($\delta^{18}O_{SMOW} \sim -23‰$) is observed in square D4 of Figure 3. Individual FeO-rich olivine grains or FeO-rich parts of the grain are smaller than 1 μm (Fig. 4b), comparable to or smaller than the interdiffusion length of Fe-Mg observed in other microobjects in this thin section. Large micro-objects (>2 μm in diameter) in the aggregate have MgO-rich cores (Fig. 4b, C3). Therefore, it is plausible that this aggregate was originally MgO-rich before Fe-Mg diffusion occurred. Thus the moderately ^{16}O-rich olivine-aggregate in region D4 (Fig. 3) was primarily a MgO-rich micro-AOA. The O-isotopic composition of the AOA was probably $\delta^{18}O_{SMOW} \sim -40‰$ at the initial stage. The primary O-isotope composition was preserved in the MgO-rich parts but

Table 4. O-isotope data (‰) of micro-objects in TTV3-1-03.[a]

Micro-object	Location in Fig. 5	Diameter/μm	$\delta^{18}O_{SMOW}$	$1\sigma_{mean}$
Ol-12 (Fo91)	D3	10	1	10
Ol-13 (Fo94)	C1	2	−2	10
Ol-14 (Fo92)	E4	4	3	10
Au-01	E3	4	6	10
Au-02	E2	4	3	10
Px-02	C3	3	−12	10
Px-03	B3	3	−5	10
Px-04	D4	2	−5	10

[a] Ol = olivine; Au = augite; Px = low-Ca pyroxene.

slightly disturbed in the FeO-rich parts due to precipitation of FeO-rich olivine along the original grain boundaries of the AOA through alteration processes in the parent body. The O-isotopic composition in the whole FeO-rich olivine aggregate is observed as $\delta^{18}O_{SMOW} \sim -23‰$ because precipitated olivine is depleted in ^{16}O. The presence of an altered micro-AOA in the matrix supports the view that ^{16}O-rich MgO-rich micro-objects in matrix are related to AOA formation.

The sizes of groundmass grains are 50 to 500 nm across (typical size, 0.2 μm; Lee et al., 1996). Because the Fe-Mg and O diffusion-lengths in olivine are estimated to be 0.5 μm and <1 nm respectively as discussed above, the diffusion processes could homogenize the Fo composition but could not homogenize the O-isotopic composition for the groundmass olivine. Therefore, individual groundmass olivine grains should have preserved the primitive O-isotopic composition at crystallization or at recrystallization.

On the other hand, presolar oxide and silicate grains having O-isotopic compositions that differ significantly from meteoritic isotope ratios have been observed (Nittler, 2003; Messenger et al., 2003; Mostefaoui et al., 2003; Nagashima et al., 2004; Nguyen and Zinner, 2004). Here we consider a case in which a 0.2 μm presolar grain with $\delta^{18}O_{SMOW} = \pm250‰$ (Messenger et al., 2003; Nittler, 2003) is embedded in the groundmass with $\delta^{18}O_{SMOW} = 0‰$. Considering each pixel size (1.25 μm) of the isotopograph and depth resolution of $\sim$50 nm in this study, we find that the extreme O-isotopic ratio of the presolar grain would be displayed as $\sim \pm6‰$ excess in the isotopograph due to O-isotopic dilution by the surrounding groundmass. This estimate indicates that such presolar grains could not be detected in the isotopographs in this study (Figs. 1, 3 and 5). Thus we cannot conclude that presolar grains in the groundmass are absent even though the isotopographs show that the O-isotope ratio in the groundmass is homogeneously distributed within $\sim \pm5‰$ (1σ) and is identical to the bulk meteoritic isotope ratio.

Because presolar oxides have been found in chondrites, we must consider two possible extreme cases to explain the homogeneous distribution of O-isotope ratios in the groundmass. One is that most minerals in the groundmass formed in the solar system and that presolar grains with extremely anomalous O-isotopic ratios are rare and widely dispersed in the groundmass. The other is that the groundmass is mostly composed of presolar grains with extremely anomalous and diverse O-isotope ratios, but that the average ratio in a 1 pixel area is equivalent to the SMOW value. Because the spatial resolution of the isotopograph is worse than the sizes of individual grains in the groundmass, we cannot determine O-isotope ratios of individual grains. However, the latter possibility may be rejected if we use the central limited theorem. We assume that the average deviation of the O-isotope ratio of presolar grains is similar to that determined in previous studies, i.e., $1\sigma \sim 250‰$ (Messenger et al., 2003; Nittler, 2003). Because the typical size of grains in the Vigarano matrix is $\sim$0.2 μm (which is comparable to presolar silicate grains reported by Messenger et al., 2003), the numbers of mineral grains in 1 pixel of the O isotopograph should be $\sim$40. Therefore, the standard deviation of the O-isotope ratio among pixels decreases from 250‰ to 40‰. The expected variation is larger than those observed in the O isotopographs in this study. Therefore, we conclude that most mineral grains of the Vigarano groundmass formed in the solar system and presolar grains would be rare. The rarity of presolar grains in the matrix of the meteorites is also supported by previous studies (e.g., Nittler et al., 1997; Strebel and Hoppe, 1999; Mostefaoui et al., 2003).

O isotopography shows that small objects that formed in different environments of the solar nebula joined together and were later incorporated into the parent body without significant alteration. Matrix material consists of different components that
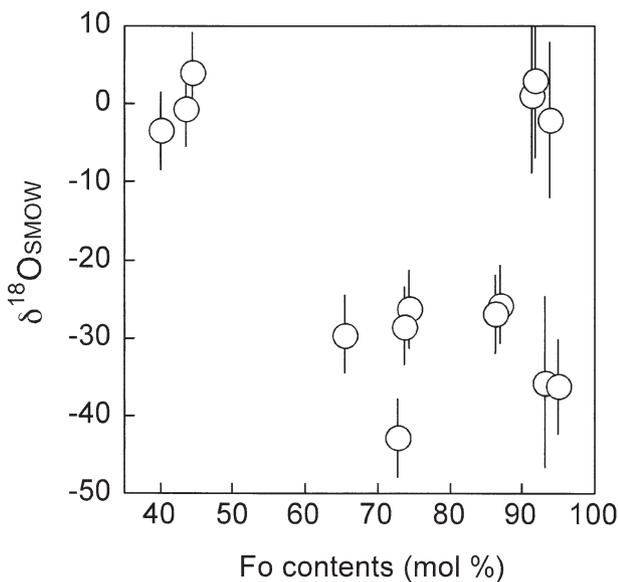

Fig. 6. $\delta^{18}O_{SMOW}$ vs. Fo content of olivine micro-objects in the Vigarano matrix. Data are from Tables 2, 3 and 4. Error bars are $1\sigma_{mean}$, which are also from Tables 2, 3, and 4.

formed in different locations and/or at different times in the nebula; matrix grains may have been derived from the AOA-CAI forming region and from the chondrule-forming region. Such nebular materials were altered in the parent body and their O-isotope signatures could have been erased through recrystallization processes. From the modal abundances of ^{16}O-rich micro-objects in the isotopographs, we conclude that at least 1% of the dust grains in the solar nebula in the CV-parent-body-formation region were enriched in ^{16}O. To reveal the exact O-isotope distribution of nebular dust and abundances of presolar grains in chondrite forming nebular region, further detailed studies of the matrices of more pristine meteorites are required.

5. CONCLUSIONS

Two-dimensional ^{18}O/^{16}O isotopic analysis of the Vigarano matrix was conducted using SIMS with SCAPS. The O-isotopic compositions of Vigarano matrix components are classified into ^{16}O-rich and ^{16}O-poor groups corresponding to $\delta^{18}O_{SMOW}$ ~ $-40‰$ and $\sim 0‰$, respectively. Oxygen isotopographs of the Vigarano matrix show that O isotopes are distributed heterogeneously in matrix material. At least 1% of the dust grains in the solar nebula were enriched in ^{16}O in the nebular region where the Vigarano parent-body formed.

There are no simple correlations between the degree of ^{16}O enrichment and the FeO content mainly because of disturbances due to Fe-Mg interdiffusion. Compositional and isotopic micro-analyses reveal that MgO-rich micro-objects have ^{16}O-rich and ^{16}O-poor compositions, whereas primary FeO-rich olivine has ^{16}O-poor composition.

The MgO-rich-olivine micro-objects are surrounded by ~1-μm thick fayalitic rims. Irregularly shaped, FeO-rich-olivine micro-objects that lack MgO-rich cores also occur in the matrix. The chemical composition of the FeO-rich-olivine micro-objects are similar to those of the fayalitic rim and groundmass olivines in the matrix, indicating chemical equilibrium. The O-isotopic composition of the FeO-rich-olivine micro-objects and groundmass olivine are depleted in ^{16}O. It is likely that the FeO-rich olivine within the matrix formed in the parent body. Hydrothermal alteration in the parent body (Krot et al., 1995, 1998) seems to be the dominant process for forming the FeO-rich micro-objects.

A FeO-rich olivine-aggregate having moderately ^{16}O-rich characteristics ($\delta^{18}O_{SMOW}$ ~ $-23‰$) was observed. The olivine aggregate was probably a MgO-rich micro-AOA. It seems that the primary O-isotope composition was preserved in the MgO-rich parts but was slightly disturbed in the FeO-rich parts because precipitated olivines were depleted in ^{16}O.

The O-isotopic composition of the groundmass in the matrix is homogeneous within ±5‰ on a micron scale. The O diffusion-length is estimated to be <1 nm from the Fe-Mg diffusion in the Vigarano parent-body. The diffusion processes could not homogenize the O-isotopic composition for the groundmass olivine. Individual groundmass olivine grains should have preserved their primitive O-isotope composition during crystallization or recrystallization. Therefore, the isotopic homogeneity of the matrix indicates that the vast majority of material in the Vigarano matrix formed in the solar system, and that presolar grains are rare.

REFERENCES

Aléon J., Engrand C., Robert F., and Chaussidon M. (2001) Clues to the origin of interplanetary dust particles from the isotopic study of their hydrogen-bearing phases. *Geochim. Cosmochim. Acta* **65,** 4399–4412.

Buening D. K. and Buseck P. R. (1973) Fe-Mg lattice diffusion in olivine. *J. Geophys. Res.* **78,** 6852–6862.

Chakraborty S. (1997) Rates and mechanisms of Fe-Mg interdiffusion in olivine at 980°–1300°C. *J. Geophys. Res.* **102,** 12317–12331.

Clayton R. N. (1993) Oxygen isotopes in meteorites. *Annu. Rev. Earth Planet. Sci.* **21,** 115–149.

Clayton R. N., Grossman L., and Mayeda T. K. (1973) A component of primitive nuclear composition in carbonaceous meteorite. *Science* **182,** 485–488.

Clayton R. N. and Mayeda T. K. (1999) Oxygen isotope studies of carbonaceous chondrites. *Geochim. Cosmochim. Acta* **63,** 2089–2104.

Gérard O. and Jaoul O. (1989) Oxygen diffusion in San Carlos olivine. *J. Geophys. Res.* **94,** 4119–4128.

Hiyagon H. and Hashimoto A. (1999) ^{16}O Excesses in olivine inclusions in Yamato-86009 and Murchison chondrites and their relation to CAIs. *Science* **283,** 828–831.

Hoppe P., Strebel R., Eberhardt P., Amari S., and Lewis R. S. (2000) Isotopic properties of silicon carbide X grains from the Murchison meteorite in the size range 0.5–1.5 μm. *Meteorit. Planet. Sci.* **35,** 1157–1176.

Imai H. and Yurimoto H. (2003) Oxygen isotopic distribution in an amoeboid olivine aggregate from the Allende CV chondrite: Primary and secondary processes. *Geochim. Cosmochim. Acta* **67,** 765–772.

Jaoul O., Froidevaux C., Durham W. B., and Michaut M. (1980) Oxygen self-diffusion in forsterite: Implications for the high-temperature creep mechanism. *Earth Planet. Sci. Lett.* **47,** 391–397.

Jaoul O., Houlier B., and Abel F. (1983) Study of ^{18}O diffusion in magnesium orthosilicate by nuclear microanalysis. *J. Geophys. Res.* **88,** 613–624.

Krot A. N., Scott E. R. D., and Zolensky M. E. (1995) Mineralogical and chemical modification of components in CV3 chondrites: Nebular or asteroidal processing? *Meteoritics* **30,** 748–775.

Krot A. N., Petaev M. I., Scott E. R. D., Choi B.-G., Zolensky M. E., and Keil K. (1998) Progressive alteration in CV3 chondrites: More evidence for asteroidal alteration. *Meteorit. Planet. Sci.* **33,** 1065–1085.

Krot A. N., McKeegan K. D., Leshin L. A., MacPherson G. J., and Scott E. R. D. (2002) Existence of an ^{16}O-rich gaseous reservoir in the solar nebula. *Science* **295,** 1051–1054.

Kunihiro T., Nagashima K., Takayanagi I., Nakamura J., Kosaka K., and Yurimoto H. (2001) Noise characteristics of stacked CMOS active pixel sensor for charged particles. *Nucl. Instr. Meth.* **A470,** 512–519.

Kunihiro T., Nagashima K., and Yurimoto H. (2002) Distribution of oxygen isotopes in matrix from the Vigarano CV3 meteorite (abstract). *Lunar Planet. Sci.* **33,** 1549.

Lee M. R., Hutchison R., and Graham A. L. (1996) Aqueous alteration in the matrix of the Vigarano (CV3) carbonaceous chondrite. *Meteorit. Planet. Sci.* **31,** 477–483.

Maruyama S., Yurimoto H., and Sueno S. (1999) Oxygen isotope evidence regarding the formation of spinel-bearing chondrules. *Earth Planet. Sci. Lett.* **169,** 165–171.

Matsumoto K., Yurimoto H., Kosaka K., Miyata K., Nakamura T., and Sueno S. (1993) A novel ion imager for secondary ion mass spectrometry. *IEEE Trans. Electron Devices* **40,** 82–85.

McKeegan K. D., Leshin L. A., Russell S. S., and MacPherson G. J. (1998) Oxygen isotopic abundances in calcium-aluminum-rich in-

clusions from ordinary chondrites: Implications for nebular heterogeneity. *Science* **280,** 414–418.

Messenger S., Keller L. P., Stadermann F. J., Walker R. M., Zinner E. (2003) Samples of stars beyond the solar system: Silicate grains in interplanetary dust. *Science* **300,** 105–108.

Mostefaoui S., Hoppe P., Marhas K. K., and Gröner E. (2003) Search for in situ presolar oxygen-rich dust in meteorites (abstract). *Meteorit. Planet. Sci.* **38,** A99.

Nagashima K., Kunihiro T., Takayanagi I., Nakamura J., Kosaka K., and Yurimoto H. (2001) Output characteristics of stacked CMOS-type active pixel sensor for charged particles. *Surf. Interface Anal.* **31,** 131–137.

Nagashima K., Krot A. N., and Yurimoto H. (2004) Stardust silicates from primitive meteorites. *Nature* **428,** 921–924.

Nguyen A. N. and Zinner E. (2004) Discovery of ancient silicate stardust in a meteorite. *Science* **303,** 1496–1499.

Nittler L. R. (2003) Presolar stardust in meteorites: Recent advances and scientific frontiers. *Earth Planet. Sci. Lett.* **209,** 259–273.

Nittler L. R., Alexander C. M. O'D., Gao X., Walker R. M., and Zinner E. K. (1994) Interstellar oxide grains from the Tieschitz ordinary chondrite. *Nature* **370,** 443–443.

Nittler L. R., Alexander C. M. O'D., Gao X., Walker R. M., and Zinner E. (1997) Stellar sapphires: The properties and origins of presolar Al_2O_3 in meteorites. *Astrophys. J.* **483,** 475–495.

Reddy K. P. R., Oh S. M., Major L. D. Jr., and Cooper A. R. (1980) Oxygen diffusion in forsterite. *J. Geophys. Res.* **85,** 322–326.

Russell S. S., MacPherson G. J., Leshin L. A., and McKeegan K. D.

(2000) ^{16}O enrichments in aluminum-rich chondrules from ordinary chondrites. *Earth Planet. Sci. Lett.* **184,** 57–74.

Ryerson F. J., Durham W. B., Cherniak D. J., and Lanford W. A. (1989) Oxygen diffusion in olivine: Effect of oxygen fugacity and implications for creep. *J. Geophys. Res. B.* **94,** 4105–4118.

Strebel R. and Hoppe P. (1999) Search for presolar oxide grains in Allende and Tieschitz residues by secondary ion imaging (abstract). *Meteorit. Planet. Sci.* **34,** A112–A113.

Takayanagi I., Nakamura J., Fossum E. R., Nagashima K., Kunihiro T., and Yurimoto H. (2003) Dark current reduction in stacked-type CMOS-APS for charged particle imaging. *IEEE Trans. Electron Devices* **50,** 70–76.

Yurimoto H., Nagasawa H., Mori Y., and Matsubaya O. (1994) Micro-distribution of oxygen isotopes in a refractory inclusion from the Allende meteorite. *Earth Planet. Sci. Lett.* **128,** 47–53.

Yurimoto H., Ito M., and Nagasawa H. (1998) Oxygen isotope exchange between refractory inclusion in Allende and solar nebula gas. *Science* **282,** 1874–1877.

Yurimoto H. and Wasson J. T. (2002) Extremely rapid cooling of a carbonaceous-chondrite chondrule containing very ^{16}O-rich olivine and a ^{26}Mg-excess. *Geochim. Cosmochim. Acta* **66,** 4355–4363.

Yurimoto H., Nagashima K., and Kunihiro T. (2003) High precision isotope micro-imaging of materials. *Appl. Surf. Sci.* **203–204,** 793–797.

Zolensky M., Barrett R., and Browning L. (1993) Mineralogy and composition of matrix and chondrule rims in carbonaceous chondrites. *Geochim. Cosmochim. Acta* **57,** 3123–3148.